

Narrow-line absorption at 689 nm in an ultracold strontium gas

Fachao Hu,^{1,2,*} Canzhu Tan,^{1,2,*} Yuhai Jiang,^{3,2,†} Matthias Weidemüller,^{1,2,4,‡} and Bing Zhu^{4,1,2,§}

¹*Hefei National Laboratory for Physical Sciences at the Microscale and Shanghai Branch, University of Science and Technology of China, Shanghai 201315, China*

²*CAS Center for Excellence and Synergetic Innovation Center in Quantum Information and Quantum Physics, University of Science and Technology of China, Shanghai 201315, China*

³*Shanghai Advanced Research Institute, Chinese Academy of Sciences, Shanghai 201210, China*

⁴*Physikalisches Institut, Universität Heidelberg, Im Neuenheimer Feld 226, 69120 Heidelberg, Germany*

(Dated: April 30, 2021)

We analyse the spectrum on the narrow-line transition $5s^2\ ^1S_0 - 5s5p\ ^3P_1$ at 689 nm in an ultracold gas of ^{88}Sr via absorption imaging. In the low saturation regime, the Doppler effect dominates in the observed spectrum giving rise to a symmetric Voigt profile. The atomic temperature and atom number can accurately be deduced from these low-saturation imaging data. At high saturation, the absorption profile becomes asymmetric due to the photon-recoil shift, which is of the same order as the natural line width. The line shape can be described by an extension of the optical Bloch equations including the photon recoil. A lensing effect of the atomic cloud induced by the dispersion of the atoms is also observed at higher atomic densities in both the low and strong saturation regimes.

I. INTRODUCTION

The existence of metastable states and narrow-line transitions among the alkaline-earth and alkaline-earth-like atoms brings new opportunities for studying cold and ultracold atoms, for example the optical-lattice clocks [1, 2], the time variation of fundamental constants [3–5], atom interferometers [6–8], nonlinear quantum optics [9–11], and strongly correlated Rydberg gases [12, 13]. While many of these applications rely on the clock transition $^1S_0 - ^3P_0$ with a linewidth on the level of mHz, the other narrow one $^1S_0 - ^3P_1$ with a ($1 \sim 100$)-kHz linewidth enable the cooling of the atoms down to the photon-recoil-limited regime [14–16] and a direct laser cooling to quantum degeneracy was demonstrated [17]. Very recently, the kHz-transitions play an essential role in the realizations of optical tweezer arrays of alkali-earth [18, 19] and alkali-earth-like [20] atoms.

Benefiting from the narrow line width of the $^1S_0 - ^3P_1$ transitions in alkali-earth or alkali-earth-like systems, fluorescence signals from these transitions can be employed for studying collective atomic scattering and motional effects [21], measuring atomic transition properties [22–24], and detecting single atoms with high fidelities [20]. On the other hand, absorption imaging using broad dipole-allowed transitions (~ 10 MHz) may be by far the most widely-used method in diagnosing ultracold-atom systems, providing accurate information on the spatial distribution of atoms, the atom number, and the atomic temperature [25, 26]. However, absorption with narrow-line transitions were rarely studied in the ultracold regime, where the photon recoil energy is comparable to the absorption linewidth including the Doppler

effect. Oates *et al.* studied the atomic-recoil-induced asymmetries in a form of saturation spectroscopy with a Ca optical-clock apparatus [27], and the photon-recoil effect on the dispersion was observed in a Yb vapor cell in Ref. [28]. Stellmer *et al.* have implemented the absorption imaging on the 7.5-kHz transition at 689 nm to resolve the hyperfine structure of the fermionic ^{87}Sr at a magnetic field of about 0.5 G [29]. They observed a Lorentzian lineshape with a full width at half maximum (FWHM) of about 40 kHz, without discussing further details on the spectrum.

In this work, we study in detail the absorption spectrum on the narrow transition $5s^2\ ^1S_0 - 5s5p\ ^3P_1$ at 689 nm with an ultracold ^{88}Sr atomic cloud. We measure the spectrum in both the weak and strong saturation regimes. At low saturations, the absorption lineshape is close to a Gaussian shape essentially determined by the Doppler effect in the temperature range studied here. Thus, this regime can be exploited for thermometry of the atomic sample, which is confirmed by a comparison to the temperature obtained by the standard time-of-flight (TOF) method [25, 26] using the broadband transition $5s^2\ ^1S_0 - 5s5p\ ^1P_1$. The narrow-line absorption imaging at low saturation also provides information on the atom numbers and atomic densities with a comparable accuracy to detection methods based on the broad (blue) line. In the strong saturation regime, an asymmetric lineshape is observed. We have performed a theoretical simulation based on the optical Bloch equations (OBEs) involving the momentum transfers during the imaging process and confirmed that the photon recoil has important influence on the line shape. We also observe a density-dependent lensing effect in the absorption images at large detunings of the imaging light.

The article is organized as follows: We show our experimental setup in Sec. II. The low- and high-saturation absorption spectra are described in Secs. III A and III B, respectively. The theoretical simulation and comparison to experiments in the high-saturation regime are discussed

* These authors contributed equally to this work.

† jiangyh@sari.ac.cn

‡ weidemueller@uni-heidelberg.de

§ bzh@physi.uni-heidelberg.de

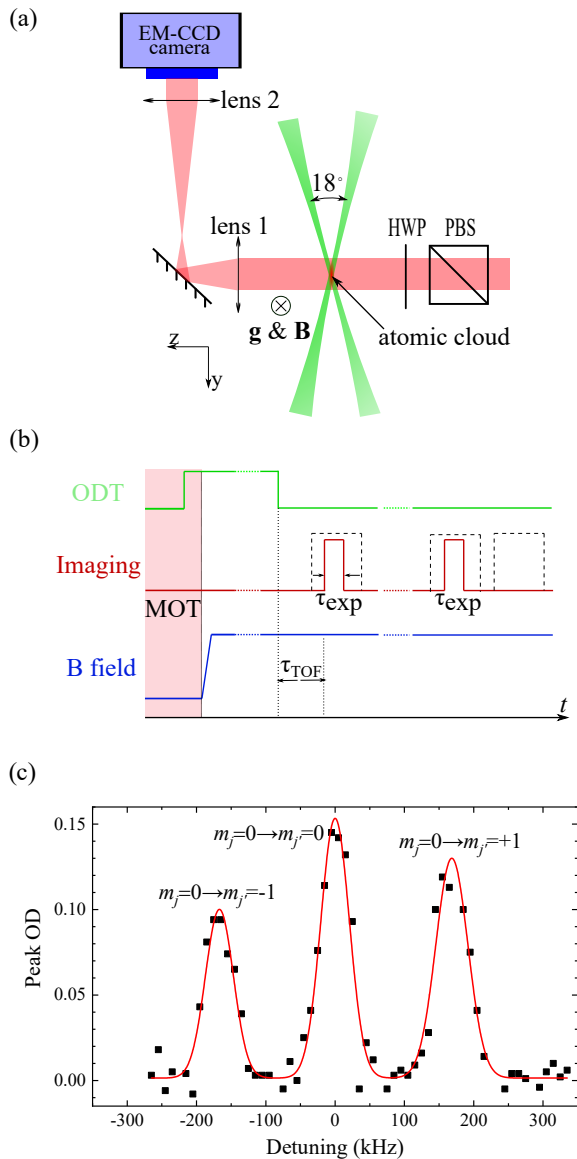


FIG. 1. (a) Schematic of the top view of experimental setup. HWP: half wave-plate; PBS: polarizing beam-splitter. \mathbf{g} and \mathbf{B} represent the gravity and magnetic field, respectively. See text for more details. (b) Time sequence for absorption imaging. See text for explanations of τ_{TOF} and τ_{exp} . (c) Absorption spectrum showing all three Zeeman sublevels of $^3\text{P}_1$ state when the imaging light polarization is tuned to about 45° angled to the residual magnetic field. Black points are the measured peak OD, and the red curve is the fit to a multi-peak Gaussian function. The obtained Zeeman splitting is $167.7(1.2)$ kHz, corresponding to a magnetic field of $79.9(6)$ mG.

in Sec. III C. The observation of lensing effect is presented in Sec. IV. Sec. V concludes the paper.

II. EXPERIMENTAL SETUP

Fig. 1(a) shows the experimental setup. The ^{88}Sr atoms are first loaded into a two-stage magneto-optical trap (MOT) for the laser cooling and trapping [30, 31], operated on the broad $5s^2^1\text{S}_0 - 5s5p^1\text{P}_1$ and narrow $5s^2^1\text{S}_0 - 5s5p^3\text{P}_1$ transitions, respectively. We could create an atomic cloud of 10^6 atoms with a density of about 10^{10} cm^{-3} and a temperature around $1 \mu\text{K}$. A cigar-shaped optical dipole trap (ODT) formed by two horizontally propagating beams at the wavelength of 532 nm , is simultaneously switched on at the second-stage MOT. The two ODT beams both have a waist of about $60 \mu\text{m}$ and cross at an angle of 18° . Holding atoms in the ODT for 200 ms to reach equilibrium after switching off the MOT, we obtain about $(0.5 \cdots 5) \times 10^5$ atoms at a temperature of $0.7 \cdots 6 \mu\text{K}$ depending on the ODT power. At a power of 0.6 W for each beam the trap depth of the ODT is about $6 \mu\text{K}$ and the trap frequencies are $2\pi \times (217, 34, 217) \text{ Hz}$ along the x , y , and z directions [see Fig. 1(a)], respectively, resulting in cloud radii of $(27, 69, 27) \mu\text{m}$ and a peak density of $7 \times 10^{11} \text{ cm}^{-3}$. The temperatures along the y and z directions are mapped out by the standard TOF method. The above-mentioned atom numbers, cloud sizes, and temperatures are measured using absorption imaging with the broad $5s^2^1\text{S}_0 - 5s5p^1\text{P}_1$ transition. The lifetime of the atomic clouds in the ODT is about 2 s , limited by the collisions with background gas.

The imaging light at 689 nm is delivered from a commercial tapered amplifier seeded by an external-cavity diode laser (Toptica TApr), used also for the narrow-line MOT cooling, which is frequency-stabilized to a passive ultra-low expansion cavity with a short-term noise of 1 kHz level and a long-term drift of 8 kHz/day [31]. As shown in Fig. 1(a), the imaging beam propagates along the z direction with a tunable linear polarization and has a $1/e^2$ diameter of 4.2 mm . The imaging pulse length and intensity are controlled by an acousto-optic modulator (not shown in the figure). The imaging system consists of two achromatic lenses with focal lengths of $+200 \text{ mm}$ and $+300 \text{ mm}$, and maps the absorption to an EM-CCD camera from Andor with a magnification factor of 1.5 . We have an imaging resolution of about $12 \mu\text{m}$.

The imaging sequence is described in Fig. 1(b). The absorption imaging on the narrow-line transition is performed after rapidly switching off the ODT to avoid the differential AC Stark shifts on the energy levels. A quantization magnetic field along the vertical direction is applied (rising time 2 ms) before the imaging pulse to split the Zeeman sublevels of $^3\text{P}_1$ state, as seen in Fig. 1(c). After a given time-of-flight (TOF) time τ_{TOF} , the atoms are shined by the imaging light with an exposure time $\tau_{\text{exp}} = 200 \mu\text{s}$. By tuning the τ_{TOF} we can tune the atomic density during the absorption, which plays an important role in observing the dispersive lensing effect discussed in Sec. III. As done in a standard absorption imaging sequence, two additional images with and with-

out the imaging light are taken after the first pulse. The three images are then processed (see, e.g., [32]) to obtain the two-dimensional optical density (OD) distribution (see the insets of Fig. 5).

By changing the linear imaging polarization angle in the $x - y$ plane, all three Zeeman sublevels of the 3P_1 state are addressable. An example is shown in Fig. 1(d). The peak OD is measured as a function of the imaging detuning showing three peaks at a magnetic field of about 80 mG. The relative line strengths are determined by the polarization and the different coupling strengths of the three corresponding transitions (see Fig. 1(d)). We have used this measurement to optimize the compensation of the background magnetic field to be better than 5 mG in our setup and to calibrate the quantization fields. For the absorption studies, we apply a field of 4 G to split the sublevels and the imaging polarization is tuned parallel to the quantization axis, so that the system is subjected only to the closed π transition ($m_j = 0 \rightarrow m_{j'} = 0$), which can be treated as a perfect two-level system.

III. MEASUREMENTS AND ANALYSIS

Thanks to the high sensitivity and large dynamical range of our imaging camera (Andor iXon 897) at 689 nm, we can study the absorption spectrum on the narrow-line transition with a saturation parameter s ranging from 0.01 to more than 100. Meanwhile, the cloud temperature and the atomic density can be controlled via the ODT depth and the TOF time τ_{TOF} independently.

A. Low-saturation absorption

In Fig. 2(a), we show two measured absorption spectra at temperatures of $1.3 \mu\text{K}$ (black points) and $5.7 \mu\text{K}$ (red points) with a saturation parameter of $s = 0.1$. The TOF time τ_{TOF} (see Fig. 1(b)) is chosen to be 3.1 ms to minimize the lensing effect (see Sec. IV) as well as to keep large enough signal-to-noise ratios (SNRs) in the OD images. The plotted signals in Fig. 1(b) are the OD integrals over the whole atomic cloud region divided by the peak cross section $\sigma_0 = 3\lambda^2/2\pi$, which is the standard way to calculate the atom number in the absorption imaging (see the following paragraph for a correction).

Symmetric lineshapes are observed in both cases and the linewidth increases with the increasing temperature. The spectra fit well to Voigt profiles with a fixed Lorentzian width of $v_L = 10.01$ kHz, resulted from the power broadening $\Gamma\sqrt{1+s}/2\pi$ and the detection bandwidth $0.9/\tau_{\text{exp}} = 4.5$ kHz due to the finite length of the square-shape imaging pulse (see Fig. 1(b)), where $\Gamma/2\pi = 7.5$ kHz is the natural linewidth. The FWHM Gaussian width v_G obtained from the Voigt profile fitting is used to deduce the temperature T_{Fit} along the imaging propagation direction, from the relation $v_G = \frac{2}{\lambda}\sqrt{2\ln 2}k_b T_{\text{Fit}}/m$. Here k_b is the Boltzmann constant, λ

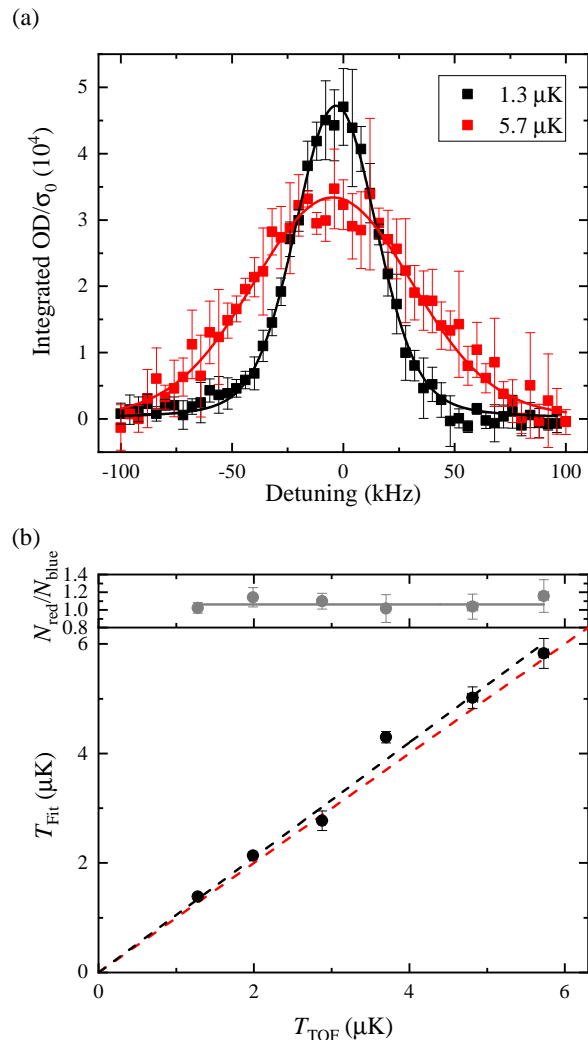


FIG. 2. (a) Low-saturation absorption spectra at temperatures of $1.3 \mu\text{K}$ (black) and $5.7 \mu\text{K}$ (red). The integrated absorption signal over the atomic cloud region is plotted as a function of the imaging detuning. The solid curves are fits to the Voigt profile. See text for more details. (b) Spectroscopic thermometry. The fitted Doppler widths from (a) are used to estimate the temperatures T_{Fit} , which are plotted against the TOF measurement results T_{TOF} in the lower panel of (b). A linear fit to the data (black dashed line) gives a slope of 1.05(3). The red dashed line represents $T_{\text{Fit}} = T_{\text{TOF}}$. In the upper panel we also show the ratio (black open circles) between the atom numbers obtained from the narrow- (N_{red}) and broad-line-width (N_{blue}) imaging, which is a constant of 1.06(2) (gray solid line).

is the transition wavelength, and m is the atomic mass. T_{Fit} obtained in this way are compared to those measured by the TOF method in the lower panel of Fig. 2(b). The linear fit between T_{Fit} and T_{TOF} (black dashed line) results in a slope of 1.05(3), which agrees excellently with the ideal case of $T_{\text{Fit}} = T_{\text{TOF}}$ (red dashed line). We also notice the empirical density broadening in the saturation fluorescence spectroscopy reported in [23]. The linear

slope is only modified slightly to 1.05(6) even if we take the empirical density relation following Ref. [23].

In addition to the temperature, the atom number and atomic density can also be extracted from the narrow-linewidth absorption imaging in the low saturation regime. The broad (blue) transition typically used in determining the atom number and atomic density has a natural linewidth on the order of 10 MHz, much broader than the Doppler width. The absorption cross-section in the broad-transition imaging can hence be regarded as temperature-independent. However, for the narrow transition with a natural linewidth smaller than the Doppler width ($\Gamma/2\pi v_G < 1$), the Doppler effect has to be considered when calculating the atom number [33]. This is done by convolving the velocity-dependent Lorentzian absorption profile with the Maxwell-Boltzmann velocity distribution in the atomic sample (see Appendix V). The convolution results in a relationship between the measured OD and the atom number similar to the broadband absorption imaging case, modified by a coefficient depending on the ratio between the Doppler-broadened width and the natural linewidth,

$$OD_0(x, y) = n(x, y)\sigma_0 \times C(\Gamma, v_G), \quad (1)$$

where $C(\Gamma, v_G) = \sqrt{\pi}\alpha e^{\alpha^2} \text{Erfc}(\alpha)$ is the coefficient with $\alpha = \sqrt{\ln 2}\Gamma/2\pi v_G$, $OD_0(x, y)$ are the on-resonance OD spatial distribution, and $n(x, y)$ is the atomic column density. $\text{Erfc}(x)$ is the complementary error function. The derivation of the coefficient is presented in the Appendix V. With the on-resonance OD and the temperature-dependent v_G determined from the spectrum fitting, the atom number and atomic density can be obtained with Eq. (1). The upper panel of Fig. 2(b) shows the ratio of the atom number determined by absorption imaging with the narrow $5s^2\ ^1S_0 - 5s5p\ ^3P_1$ (N_{red}) and broad $5s^2\ ^1S_0 - 5s5p\ ^1P_1$ (N_{blue}) transitions, which lies close to 1 (gray solid line).

B. Strong-saturation absorption

In this section we study the narrow-line absorption spectrum at strong saturations with $s \gg 1$. The question arises, to which extent the photon recoils impacts the absorption profile, as the the recoil shift is comparable to the natural linewidth (~ 4.78 kHz vs. 7.5 kHz for the narrow transition studied here). During the absorption process, absorption and spontaneous emission events give rise to the change of momentum distribution, and hence affecting the subsequent absorption. For narrow-line transitions, few photon-recoil events are enough to drive the atom out of resonance with the imaging laser. This is in stark contrast to broadband transitions, since the natural linewidth is usually much larger than the Doppler shifts induced by photon recoils in a cold atom sample. Nevertheless, the photon-recoil effect was already considered when imaging light species like Li using

broad transitions [34], where the recoil-induced detuning and blurring place strong constraints on the proper imaging conditions.

In Fig. 3(a) we show two absorption spectra at saturation parameters of $s = 0.09$ and $s = 35.8$, respectively. We observe a decrease of the integrated OD signal at all detunings due to the saturation effect (note that the data at higher saturation is magnified by a factor of 6 for a better view). More importantly, the lineshape is asymmetric at the high saturation, namely the integrated OD approaches zero more slowly on the negative-detuning side than that on the positive one, and the absorption peak is shifted by a few kHz to the positive detuning. At high saturation, differences can already be seen in the OD images at the two detuning sides [see lower rows in the insets of Figs. 3(b-d)], namely a wider spatial extension for the position detuning than that for the negative one. In this series of experiments, the influence of the lensing effect on the OD measurement (see Sec. IV) is negligible due to the low atomic densities involved here.

The observed asymmetry and peak shift can be interpreted qualitatively by considering the absorption process including the influence of the photon recoil. The photon recoil associated with each absorption-spontaneous emission cycle redistributes the momentum of atoms, which depends strongly on the light detuning [35]. Consequently, an asymmetric lineshape and the shift of the maximum of absorption emerges when more and more photons are scattered due to the momentum redistribution in the atomic cloud. In order to resolve such effects, the Doppler width has to be comparable to the power-broadened line width. In the case of the strong saturation in Fig. 3 (a), the power-broadened Lorentzian width $\Gamma\sqrt{1+s} \sim 45$ kHz is close to the Doppler one of ~ 40 kHz. In the following subsection a quantitative description is presented incorporating the photon-recoil effect in an OBE formalism.

C. Spectrum lineshape simulation

We take an OBE formalism including the method of so-called 'momentum families' from Ref. [36], originally developed to understand laser cooling on a narrow-line transition. The model considers a two-level atom system with an initial Maxwell-Boltzmann thermal distribution, interacting with a single near-resonant monochromatic homogeneous probe beam. The state of an atom with momentum \mathbf{p} is expressed in the form of $\{|g, \mathbf{p}\rangle, |e, \mathbf{p}\rangle\}$, where $|g(e)\rangle$ corresponds to the atomic ground (excited) state. The system Hamiltonian driven under a laser beam propagating along the z axis is,

$$H_0 = \frac{\hat{\mathbf{p}}^2}{2m} + \hbar\omega_0 |e\rangle\langle e| - \hat{\mathbf{D}} \cdot \hat{\mathbf{E}} \quad (2)$$

where ω_0 , $\hat{\mathbf{D}}$, $\hat{\mathbf{E}}$ are the transition frequency, dipole moment operator, and laser electric field, respectively. In

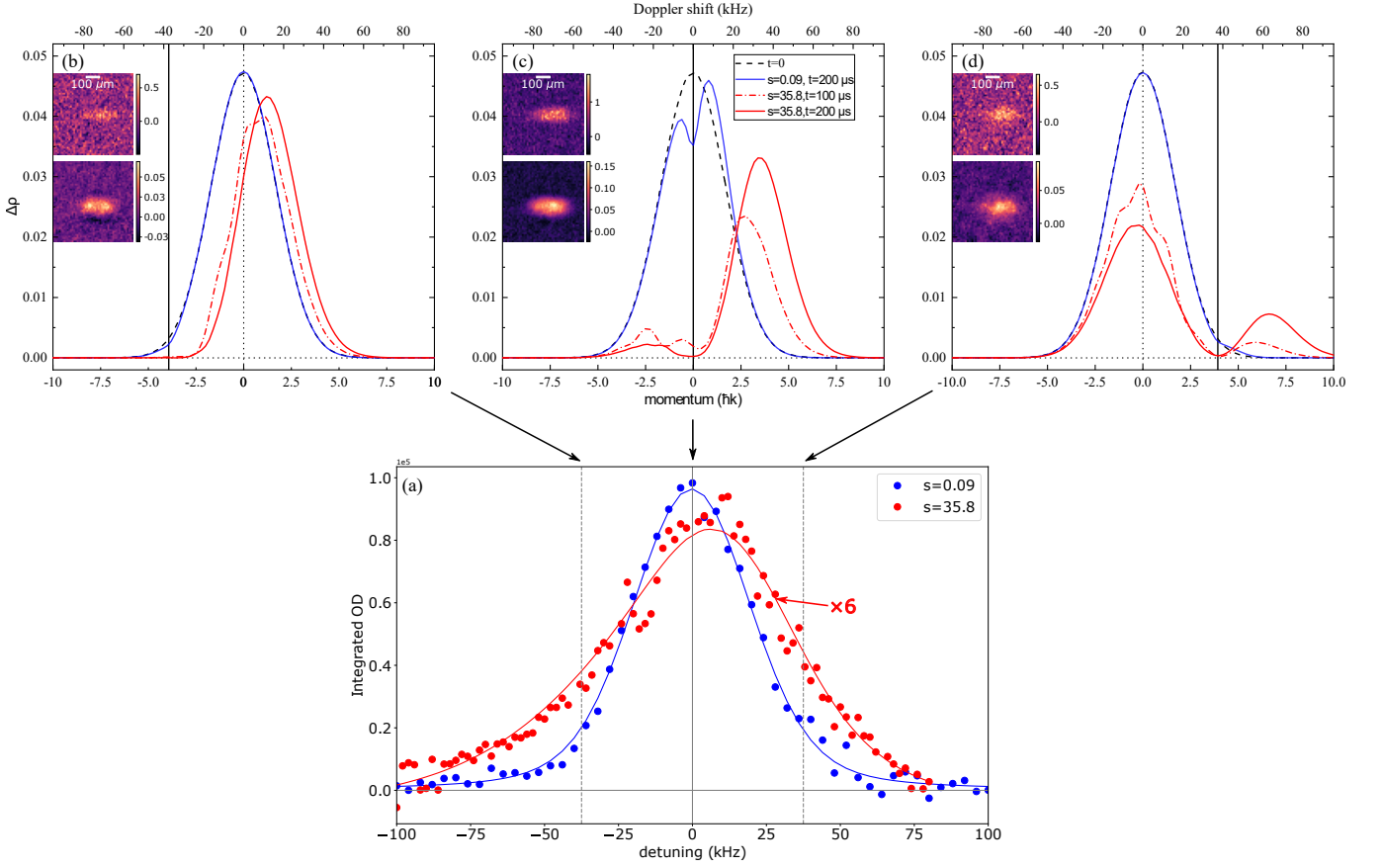


FIG. 3. High-saturation absorption. (a) The measured absorption lineshapes at low (blue dots) and high (red dots) saturations. The data in the high-saturation case ($s = 35.8$) showing asymmetric profile is fitted to the numerical solution of Eq. (5) (red curve) and magnified by 6 times to have a better visualization. As a comparison, the low-saturation ($s = 0.09$) data is symmetric and fits well to the Voigt profile (blue curve). (b) - (d), the population difference $\Delta\rho(p)$ obtained from the OBE solutions at there different detunings [$0, \pm 5\Gamma$, as marked by the grey vertical lines in (a)] after an exposure time of $100\ \mu\text{s}$ and $200\ \mu\text{s}$, respectively. As a reference, we also show the initial distribution at $t = 0$, which is the Maxwell-Boltzmann one determined by the cloud temperature. The black solid vertical lines mark the resonant momentum positions, where the probe detuning is compensated by the Doppler effect. The inset images show measurements of the two-dimensional OD distributions at low (upper) and high (lower) saturations for their respective detunings.

our case, only the π -transition branch $m_j = 0 \rightarrow m_{j'} = 0$ is considered, and only momentum along the light propagation axis $p = p_z$ is preserved, with the other two components p_x, p_y traced over. The system Hamiltonian under the rotating-wave approximation becomes,

$$H_S = \frac{\hat{p}^2}{2m} - \hbar\delta |e\rangle \langle e| + \frac{\hbar\Omega}{2} (e^{ikz} |e\rangle \langle g| + |g\rangle \langle e| e^{-ikz}) \quad (3)$$

where δ, Ω are the bare detuning and Rabi frequency.

The evolution of states $|g, p\rangle, |e, p + \hbar k\rangle$ with any momentum p remains globally closed under H_S when the spontaneous emission is not considered, for which reason the states $|g, p\rangle, |e, p + \hbar k\rangle$ are grouped as a family $\mathcal{F}(p)$. The system density matrix ρ expanded in this basis is,

$$\begin{aligned} \rho_{gg}(p) &= \langle g, p | \rho | g, p \rangle \\ \rho_{ee}(p) &= \langle e, p + \hbar k | \rho | e, p + \hbar k \rangle \\ \rho_{ge}(p) &= \rho_{eg}^*(p) = \langle g, p | \rho | e, p + \hbar k \rangle \end{aligned} \quad (4)$$

The equations of evolution under H_S together with the spontaneous emission processes are,

$$\begin{aligned} \dot{\rho}_{gg}(p) &= \Gamma \bar{\pi}_e (p - \hbar k) - \frac{i\Omega}{2} (\rho_{eg}(p) - \rho_{ge}(p)), \\ \dot{\rho}_{ee}(p) &= -\Gamma \bar{\pi}_e (p) + \frac{i\Omega}{2} (\rho_{eg}(p) - \rho_{ge}(p)), \\ \dot{\rho}_{ge}(p) &= \dot{\rho}_{eg}^*(p) \\ &= -(i(\bar{\delta} - \frac{kp}{m}) + \frac{\Gamma}{2}) \rho_{ge}(p) + \frac{i\Omega}{2} (\rho_{gg}(p) - \rho_{ee}(p)), \end{aligned} \quad (5)$$

where $\bar{\delta} = \delta - \hbar k^2 / (2m)$ and the term $\bar{\pi}_e$ represents the impact of spontaneous decay on the system evolution,

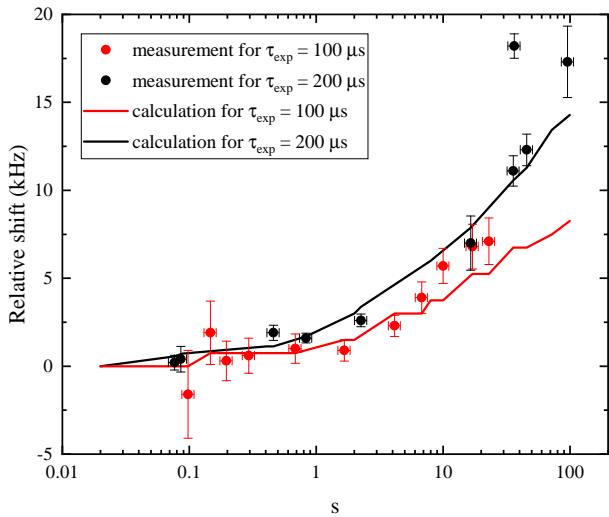


FIG. 4. Absorption peak position shift. The relative position of the absorption peak at different saturation parameters s are compared for imaging times of $100 \mu\text{s}$ (red circles and curve) and $200 \mu\text{s}$ (black circles and curve). The black and red curves are the calculated results without any free parameters, while the black and red circles are the fitted results from measurements by using the peak position and height as the two free fitting parameters. See text for more discussions.

defined as

$$\bar{\pi}_e(p) = \int_{-\infty}^{+\infty} dp_x \int_{-\infty}^{+\infty} dp_y \int_{-\hbar k}^{+\hbar k} dp'_z \mathcal{N}(p') \langle e, p_x, p_y, p_z = p + p' | \rho | e, p_x, p_y, p_z = p + p' \rangle. \quad (6)$$

Here $\mathcal{N}(p') = \frac{3}{4\hbar k} (1 - p'^2/\hbar^2 k^2)$ results from the classical dipole radiation pattern [36] of the π transition. With all the atoms initially at the ground state $|g\rangle$ with a Maxwell-Boltzmann distribution of temperature T , we numerically integrate the equations (5) to get the system evolution. The solution of the off-diagonal elements $\rho_{eg}(p)$ results in the susceptibility $\chi(p) \propto n\rho_{eg}(p)$ with the atomic density n . The absorption profile is then calculated by tracing the imaginary part of the susceptibility over all momenta, i.e. $\sum_p \text{Im}\chi(p)$, and then integrating over the interaction duration.

For the solid curves in Figs. 3(a), we fit the experimental data to the calculated profiles with the maximum integrated OD and the peak position as the only free parameters. Both the lineshape asymmetry and the shift of the absorption peak at high saturation can be reproduced very well by Eq. (5) including the momentum transfer due to the photon-scattering events. While the model predicts a significant shift of the absorption peak, its position is still used as a free parameter in the fits to account for the possible deviation between the measurements and the calculations, as discussed in more details in Fig. 4.

One can gain further insight into the photon-recoil effects by considering the quasi-steady solution of the off-diagonal element in Eq. (5), $\text{Im}\rho_{eg}(p) \propto \Delta\rho(p) = \rho_{gg}(p) - \rho_{ee}(p)$. We show from Fig. 3(b) to 3(d) the calculated distribution of the population difference $\Delta\rho(p)$ at two saturation parameters of $s \approx 0.09$ (blue curves) and $s = 35.8$ (red curves) after $200\text{-}\mu\text{s}$ atom-light interaction time (about $10/\Gamma$, the imaging pulse length in this measurement), when the probe laser is detuned by $-5\Gamma, 0, +5\Gamma$ from left to right. At the low saturation ($s \approx 0.09$), $\Delta\rho(p)$ is only slightly modified compared to the initial Maxwell-Boltzmann distribution (black dot-dashed lines), remaining almost Gaussian even after long interaction time, such that the convolution between the velocity-dependent Lorentzian profile. The momentum distribution results in a lineshape nearly the Voigt one, as the blue curve seen in Fig. 3(a). When highly saturated ($s = 35.8$), however, the $\Delta\rho(p)$ distribution is strongly modified and depleted near the resonant momentum (marked by vertical dashed lines) where the Doppler shift compensates the bare imaging detuning. In Fig. 3(b) with a detuning of -5Γ , the distribution maintains a Gaussian shape with the center shifted by $\sim 1.2\hbar k$ after $200 \mu\text{s}$. While at a detuning of $+5\Gamma$ in Fig. 3(d), two peaks appear on the opposite sides of the resonant momentum. Such a strong dependence on the detuning leads to the observed asymmetric lineshape and the peak shift.

The effects of the photon recoil can also be revealed by studying the time evolution of the momentum distribution. In Figs. 3(b-d) the $\Delta\rho(p)$ at $s = 35.8$ after $100\text{-}\mu\text{s}$ interaction (red dash-dot curves) are shown as a comparison to the $200\text{-}\mu\text{s}$ case. Small but clear differences of $\Delta\rho(p)$ are observed for all three detunings indicating that the momentum distribution undergoes some time evolution, which may result in a time-dependent absorption lineshape. This is actually demonstrated in Fig. 4 by comparing the saturation-dependent shift of the absorption peak position for the 100- and $200\text{-}\mu\text{s}$ imaging durations. The peak position is shifted towards the positive detuning when increasing the imaging intensity and such a shift becomes larger in the case of a longer exposure, i.e. more photons are scattered. The solid curves represent the calculated results without any free parameters, while the solid dots are from fits with the peak position and height as the free fitting parameters [see Fig. 3(a)]. Overall, the fitted shifts agree well with the calculations without free parameters, while deviations are seen for some points coming from fluctuations of experimental conditions like laser power and atom number, as well as the low SNR for large saturation parameters.

IV. THE LENSING EFFECT

As shown in Fig. 5, we have also experimentally observed another phenomenon in the absorption spectrum at high atomic densities, the so-called lensing ef-

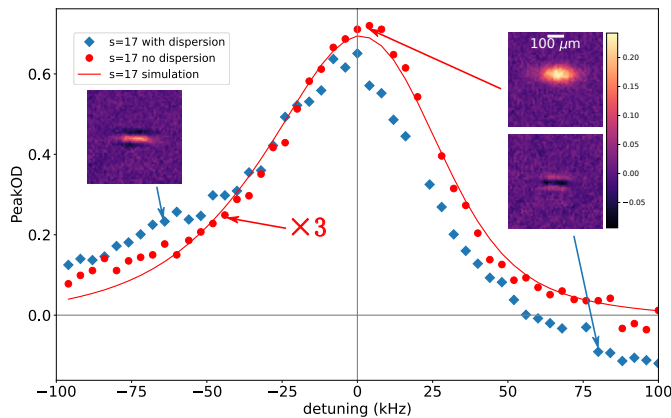


FIG. 5. Absorption spectrum with $s = 17$ at two different atomic densities of $8.9 \times 10^{10} \text{ cm}^{-3}$ (red circles) and $2.8 \times 10^{11} \text{ cm}^{-3}$ (blue diamonds). The red curve is a fit to the numerical solution of Eq. (5). We obtain negative peak ODs at some large positive detunings. In the right inset, the lower OD image measured at a large positive detuning with the high atomic density has a dark hole instead of a bright peak in the cloud center, caused by the lensing effect. At the large negative detuning, the dark position appears at the edges of the cloud (left inset). As a comparison, we also show an example of the OD images for the low-density case with a normal Gaussian distribution in the upper panel of the inset.

fact which is well known in standard absorption imaging. The absorption spectra at two different atomic densities are compared at a saturation of $s = 17$. In the low-density case ($n \sim 8.9 \times 10^{10} \text{ cm}^{-3}$, red dots in the figure), we find a similar asymmetry as that in Fig. 3(a) for the high saturation. With a 3-fold higher density ($n \sim 2.8 \times 10^{11} \text{ cm}^{-3}$, blue diamonds in the figure), a negative peak OD is obtained from the two-dimension Gaussian fit at some large positive detunings. Checking the OD images there (one example shown as the right inset in Fig. 5), a dark hole instead of a bright peak is seen at the central region of the atomic cloud for the large positive detuning, while at the negative one a dark edge is observed. This phenomenon is related to the microscopic lensing effect studied in e.g. Refs. [37–43], where a spatial-dependent index of refraction leads to a focusing or defocusing effect on the imaging beam depending on the detuning.

The observed lensing effect can be understood from the following equation for describing the phase shift of the imaging field in the transverse plane propagating through a cloud of two-level atoms [39],

$$d\phi(x, y) = -\sigma_0 n(x, y, z) dz \frac{\delta/\Gamma}{1 + 4(\delta/\Gamma)^2 + s(x, y)}. \quad (7)$$

Here dz is the thickness of the atomic cloud along the light propagation direction, δ is the detuning, and $s(r)$ has a spatial dependence due to the intensity distribution of a Gaussian probe beam. Spatial inhomogeneity of the index of refraction can be induced by the spatial

distribution of the atomic density, or the probe intensity, or both. For negative (positive) detuning, Eq. (7) leads to a focusing (defocusing) of the imaging beam.

The observed lensing effect here mainly stems from the density inhomogeneity as indicated by the density-dependence (see Fig. 5) and the fact that the imaging beam is much larger than the atomic cloud (~ 200 times). The lensing induced by such density inhomogeneity was observed in both the weak- [40] and strong-saturation [37–39] regimes. The lensing effect shown in Fig. 5 with strong saturation is also observable in the weak-probe case in our experiment. However, to quantitatively explain our observation, detailed calculations on the light propagation are needed like in Refs. [41, 43], even including the atom dipolar interactions or multiple scattering events (e.g. [21, 44, 45]), which is beyond the scope of this paper.

V. CONCLUSION

In conclusion, we have studied both experimentally and theoretically the absorption spectrum of a narrow-line transition at 689 nm in an ultracold ^{88}Sr gas. The atomic cloud temperature down to $1 \mu\text{K}$ can be inferred from the measured absorption lineshape at low probe saturations ($s \ll 1$) if the Doppler width dominates over other line-broadening effects. Information on the atom number can also be reliably extracted from the low-saturation absorption. In the strongly saturated regime, we observed the photon-recoil-induced asymmetry in the absorption spectrum, which can be described by two-level OBEs involving the photon recoils. We also showed a lensing effect when probing a high-density sample, which is due to the spatial-dependent dispersive response of the atomic cloud to the imaging field. It is of strong interest in studying further the weak-probe high-density regime because of the collective and cooperative effects that are predicted theoretically [44, 46–48]. The narrow-line absorption can also be employed as sensitive probe for other cold atom systems with similar narrow-line transitions, like, e.g., Yb. The good resolution also makes the narrow-line absorption applicable to detection of interactions in more complicated systems, e.g. the spatial correlation [49] due to Rydberg blockade.

ACKNOWLEDGEMENTS

We acknowledge C. Qiao, L. Couturier, and I. Nosske for their contributions on setting up the experiment at the early stage of project. F.H acknowledges Yaxiong Liu for helpful discussions on numerical algorithms. M.W.’s research activities in China are supported by the 1000-Talent-Program. The work was supported by the National Natural Science Foundation of China (Grant Nos. 11574290 and 11604324) and Shanghai Natural Science

Foundation (Grant No. 18ZR1443800). Y.H.J. also acknowledges support under Grant No. 11827806.

APPENDIX

The low-saturation ($s \ll 1$) OD spatial distribution is represented as,

$$OD(x, y) = \int_{-\infty}^{+\infty} \sigma_0 n(x, y) f(v) L(\delta, v, \Gamma) dv \quad (8)$$

where $L(\delta, v, \Gamma) = \frac{\Gamma^2/4}{(\delta - kv)^2 + \Gamma^2/4}$ is the Lorentzian profile with δ the bare laser detuning, Γ the natural linewidth, $k = 2\pi/\lambda$ the laser wavenumber, and v the atom velocity, $f(v) = \frac{1}{u\sqrt{\pi}} e^{-v^2/u^2}$ is the Gaussian velocity distribution with $u = \sqrt{2k_B T/m}$ the most probable speed. The Doppler width v_G is related to u , $v_G = ku\sqrt{\ln 2}/\pi$. Then

Eq. (8) reads

$$\begin{aligned} OD(x, y) &= \sigma_0 n(x, y) \int_{-\infty}^{+\infty} \frac{1}{u\sqrt{\pi}} e^{-(v/u)^2} \frac{\Gamma^2/4}{(\delta - kv)^2 + \Gamma^2/4} dv \\ &= \sigma_0 n(x, y) \frac{\alpha^2}{\sqrt{\pi}} \int_{-\infty}^{+\infty} \frac{e^{-(x' + \delta/ku)^2}}{x'^2 + \alpha^2} dx' \end{aligned} \quad (9)$$

The substitution $x' \equiv kv - \delta$ is used in the second step. Here $\alpha = \frac{\sqrt{\ln 2} \Gamma}{2\pi v_G}$ represents the ratio between the natural linewidth and the Doppler width. At the on-resonance condition ($\delta = 0$) we have the Eq. (1). The coefficients $C(\Gamma, v_G) = \sqrt{\pi} \alpha e^{\alpha^2} \text{Erfc}(\alpha)$ for correcting the on-resonance absorption cross section are plotted in Fig. for the $5s^2 \ ^1S_0 - 5s5p \ ^1P_1$ (black dashed line), $5s^2 \ ^1S_0 - 5s5p \ ^3P_1$ (blue dashed line) transitions of ^{88}Sr and the D2 transition of ^{87}Rb (red dotted line) as a comparison.

-
- [1] H. K. Jun Ye, H. J. Kimble, *Science* (2008), [10.1126/science.1148259](#).
- [2] A. D. Ludlow, M. M. Boyd, J. Ye, E. Peik, and P. Schmidt, *Reviews of Modern Physics* **87**, 637 (2015).
- [3] M. Safronova, D. Budker, D. DeMille, D. F. J. Kimball, A. Derevianko, and C. W. Clark, *Reviews of Modern Physics* **90** (2018), [10.1103/RevModPhys.90.025008](#).
- [4] M. S. Safronova, S. G. Porsev, C. Sanner, and J. Ye, *Physical Review Letters* **120** (2018), [10.1103/physrevlett.120.173001](#).
- [5] C. J. Kennedy, E. Oelker, J. M. Robinson, T. Bothwell, D. Kedar, W. R. Milner, G. E. Marti, A. Derevianko, and J. Ye, *Physical Review Letters* **125** (2020), [10.1103/physrevlett.125.201302](#).
- [6] L. Hu, N. Poli, L. Salvi, and G. M. Tino, *Physical Review Letters* **119** (2017), [10.1103/physrevlett.119.263601](#).
- [7] L. Hu, E. Wang, L. Salvi, J. N. Tinsley, G. M. Tino, and N. Poli, *Classical and Quantum Gravity* **37**, 014001 (2019).
- [8] J. Rudolph, T. Wilkason, M. Nantel, H. Swan, C. M. Holland, Y. Jiang, B. E. Garber, S. P. Carman, and J. M. Hogan, *Physical Review Letters* **124** (2020), [10.1103/physrevlett.124.083604](#).
- [9] J. Ye, L.-S. Ma, and J. L. Hall, *Journal of the Optical Society of America B* **15**, 6 (1998).
- [10] B. T. R. Christensen, M. R. Henriksen, S. A. Schäffer, P. G. Westergaard, D. Tieri, J. Ye, M. J. Holland, and J. W. Thomsen, *Physical Review A* **92** (2015), [10.1103/physreva.92.053820](#).
- [11] P. G. Westergaard, B. T. Christensen, D. Tieri, R. Martin, J. Cooper, M. Holland, J. Ye, and J. W. Thomsen, *Physical Review Letters* **114** (2015), [10.1103/physrevlett.114.093002](#).
- [12] F. B. Dunning, T. C. Killian, S. Yoshida, and J. Burgdörfer, *Journal of Physics B: Atomic, Molecular and Optical Physics* **49**, 112003 (2016).
- [13] I. S. Madjarov, J. P. Covey, A. L. Shaw, J. Choi, A. Kale, A. Cooper, H. Pichler, V. Schkolnik, J. R. Williams, and

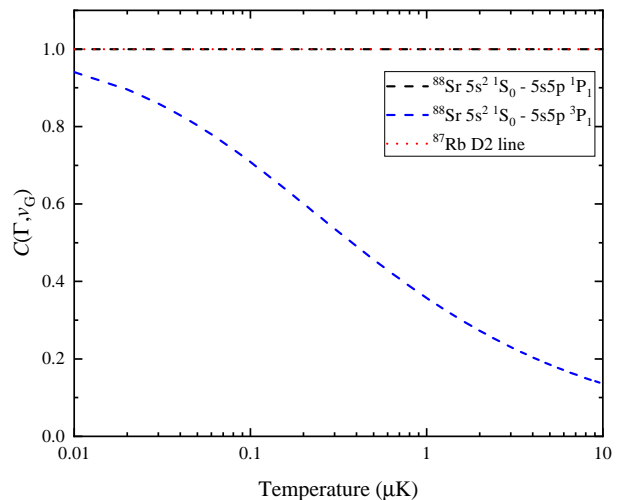


FIG. 6. The coefficient for correcting the on-resonance absorption cross section due to the Doppler effect. The plotted temperature range is 0.01 – 10 μK . Three atomic transitions are compared: the broad $5s^2 \ ^1S_0 - 5s5p \ ^1P_1$ (black dashed line) and narrow $5s^2 \ ^1S_0 - 5s5p \ ^3P_1$ (blue dashed line) transitions in ^{88}Sr , and the D2 line of ^{87}Rb (red dotted line). This coefficient is 1 for broad transitions ($\Gamma \gg 2\pi v_G$) and strongly modified for narrow ones ($\Gamma \lesssim 2\pi v_G$) in the ultracold range.

- M. Endres, *Nature Physics* (2020), [10.1038/s41567-020-0903-z](#).
- [14] E. A. Curtis, C. W. Oates, and L. Hollberg, *Phys. Rev. A* **64**, 031403 (2001).
- [15] T. H. Loftus, T. Ido, A. D. Ludlow, M. M. Boyd, and J. Ye, *Physical Review Letters* **93** (2004), [10.1103/physrevlett.93.073003](#).
- [16] A. Guttridge, S. A. Hopkins, S. L. Kemp, D. Boddy, R. Freytag, M. P. A. Jones, M. R. Tarbutt, E. A. Hinds,

- and S. L. Cornish, *Journal of Physics B: Atomic, Molecular and Optical Physics* **49**, 145006 (2016).
- [17] S. Stellmer, B. Pasquiou, R. Grimm, and F. Schreck, *Physical Review Letters* **110** (2013), [10.1103/physrevlett.110.263003](https://doi.org/10.1103/physrevlett.110.263003).
- [18] M. A. Norcia, A. W. Young, and A. M. Kaufman, *Physical Review X* **8**, 041054 (2018).
- [19] A. Cooper, J. P. Covey, I. S. Madjarov, S. G. Porsev, M. S. Safronova, and M. Endres, *Physical Review X* **8** (2018), [10.1103/physrevx.8.041055](https://doi.org/10.1103/physrevx.8.041055).
- [20] S. Saskin, J. Wilson, B. Grinkemeyer, and J. Thompson, *Physical Review Letters* **122** (2019), [10.1103/physrevlett.122.143002](https://doi.org/10.1103/physrevlett.122.143002).
- [21] S. L. Bromley, B. Zhu, M. Bishof, X. Zhang, T. Bothwell, J. Schachenmayer, T. L. Nicholson, R. Kaiser, S. F. Yelin, M. D. Lukin, A. M. Rey, and J. Ye, *Nature Communications* **7** (2016), [10.1038/ncomms11039](https://doi.org/10.1038/ncomms11039).
- [22] G. Ferrari, P. Cancio, R. Drullinger, G. Giusfredi, N. Poli, M. Prevedelli, C. Toninelli, and G. M. Tino, *Physical Review Letters* **91** (2003), [10.1103/physrevlett.91.243002](https://doi.org/10.1103/physrevlett.91.243002).
- [23] T. Ido, T. H. Loftus, M. M. Boyd, A. D. Ludlow, K. W. Holman, and J. Ye, *Physical Review Letters* **94** (2005), [10.1103/physrevlett.94.153001](https://doi.org/10.1103/physrevlett.94.153001).
- [24] M. Schmitt, E. A. L. Henn, J. Billy, H. Kadau, T. Maier, A. Griesmaier, and T. Pfau, *Opt. Lett.* **38**, 637 (2013).
- [25] W. Ketterle, D. S. Durfee, and D. Stamper-Kurn, arXiv preprint cond-mat/9904034 (1999).
- [26] W. Ketterle and M. W. Zwierlein, arXiv preprint arXiv:0801.2500 (2008).
- [27] C. Oates, G. Wilpers, and L. Hollberg, *Physical Review A* **71** (2005), [10.1103/physreva.71.023404](https://doi.org/10.1103/physreva.71.023404).
- [28] R. Grimm and J. Mlynek, *Physical Review Letters* **61**, 2308 (1988).
- [29] S. Stellmer, R. Grimm, and F. Schreck, *Physical Review A* **84** (2011), [10.1103/physreva.84.043611](https://doi.org/10.1103/physreva.84.043611).
- [30] I. Nosske, L. Couturier, F. Hu, C. Tan, C. Qiao, J. Blume, Y. H. Jiang, P. Chen, and M. Weidemüller, *Physical Review A* **96** (2017), [10.1103/physreva.96.053415](https://doi.org/10.1103/physreva.96.053415).
- [31] C. Qiao, C. Z. Tan, F. C. Hu, L. Couturier, I. Nosske, P. Chen, Y. H. Jiang, B. Zhu, and M. Weidemüller, *Applied Physics B* **125** (2019), [10.1007/s00340-019-7328-3](https://doi.org/10.1007/s00340-019-7328-3).
- [32] H. J. Lewandowski, D. Harber, D. L. Whitaker, and E. A. Cornell, *Journal of low temperature physics* **132**, 309 (2003).
- [33] C. Foot, *Atomic Physics* (Oxford University Press, 2004).
- [34] M. Horikoshi, A. Ito, T. Ikemachi, Y. Aratake, M. Kuwata-Gonokami, and M. Koashi, *Journal of the Physical Society of Japan* **86**, 104301 (2017).
- [35] S. Stenholm, *Applied Physics* **15**, 287 (1978).
- [36] Y. Castin, H. Wallis, and J. Dalibard, *Journal of the Optical Society of America B* **6**, 2046 (1989).
- [37] G. Labeyrie, T. Ackemann, B. Klappauf, M. Pesch, G. Lippi, and R. Kaiser, *The European Physical Journal D-Atomic, Molecular, Optical and Plasma Physics* **22**, 473 (2003).
- [38] Y. Wang and M. Saffman, *Phys. Rev. A* **70**, 013801 (2004).
- [39] G. Labeyrie, G. Gattobigio, T. Chanelière, G. Lippi, T. Ackemann, and R. Kaiser, *The European Physical Journal D* **41**, 337 (2007).
- [40] S. Roof, K. Kemp, M. Havey, I. M. Sokolov, and D. V. Kupriyanov, *Opt. Lett.* **40**, 1137 (2015).
- [41] J. Han, T. Vogt, M. Manjappa, R. Guo, M. Kiffner, and W. Li, *Physical Review A* **92** (2015), [10.1103/physreva.92.063824](https://doi.org/10.1103/physreva.92.063824).
- [42] M. Noaman, M. Langbecker, and P. Windpassinger, *Opt. Lett.* **43**, 3925 (2018).
- [43] J. R. Gilbert, C. P. Roberts, and J. L. Roberts, *J. Opt. Soc. Am. B* **35**, 718 (2018).
- [44] B. Zhu, J. Cooper, J. Ye, and A. M. Rey, *Physical Review A* **94** (2016), [10.1103/physreva.94.023612](https://doi.org/10.1103/physreva.94.023612).
- [45] J. Chabé, M.-T. Rouabah, L. Bellando, T. Bienaimé, N. Piovella, R. Bachelard, and R. Kaiser, *Physical Review A* **89** (2014), [10.1103/physreva.89.043833](https://doi.org/10.1103/physreva.89.043833).
- [46] T. Bienaimé, R. Bachelard, N. Piovella, and R. Kaiser, *Fortschritte der Physik* **61**, 377 (2013).
- [47] D. Kupriyanov, I. Sokolov, and M. Havey, *Physics Reports* **671**, 1 (2017).
- [48] R. J. Bettles, M. D. Lee, S. A. Gardiner, and J. Ruostekoski, *Communications Physics* **3**, 1 (2020).
- [49] G. Günter, M. R. de Saint-Vincent, H. Schempp, C. S. Hofmann, S. Whitlock, and M. Weidemüller, *Physical Review Letters* **108** (2012), [10.1103/physrevlett.108.013002](https://doi.org/10.1103/physrevlett.108.013002).